

Heavy Flavor Production in PHENIX

Olivier Drapier, on behalf of the PHENIX collaboration

LLR-École Polytechnique, Palaiseau, France

Received: date / Revised version: date

Abstract. The PHENIX experiment at RHIC measured single electron spectra in p+p, d+Au and Au+Au collisions at $\sqrt{s_{NN}} = 200$ GeV, and in Au+Au collisions at $\sqrt{s_{NN}} = 62.4$ GeV. In these spectra, electrons from semi-leptonic decays of charmed particles are the dominant contribution after subtraction of all 'photonic' sources (photon conversions, Dalitz decays, decays of light vector mesons). The p+p open charm production cross-section is found to be in good agreement with pQCD NLO calculations. The shape of the distributions obtained for p+p interactions is compared with those observed for nucleus-nucleus collisions. From p+p to d+Au and Au+Au interactions, open charm production is found to scale with the number of binary collisions N_{coll} . Au+Au data at $\sqrt{s_{NN}} = 62.4$ GeV is compatible with the ISR p+p results scaled by N_{coll} . The elliptic flow parameter v_2 of heavy flavor electrons has also been measured, and is found to be non-zero in the intermediate p_T range.

PACS. 25.75-q Relativistic heavy-ion collisions – 25.75.Dw Particle and resonance production

1 Introduction

The measurement of heavy flavor quark production is of key importance for the study of high energy nucleus-nucleus collisions, for several reasons:

- Production of heavy quark-antiquark pair resonances, such as J/ψ and \mathcal{T} 's has been proposed as a probe of the hot and dense medium created in high energy nucleus-nucleus interactions. In the original model by T. Matsui and H. Satz [1], the quark-antiquark potential is screened by the color charge density of the medium, preventing the pair from evolving towards a bound state. Other calculations [2] predict an increase of heavy quarkonia production, due to coalescence. Whereas an anomalous suppression [3] of J/ψ has been observed in Pb+Pb collisions at CERN energies ($\sqrt{s_{NN}} \simeq 18$ GeV), charmonium measurements with heavy ions at RHIC [4] did not allow to draw any conclusion yet, because of low statistics.

- At RHIC energies, heavy flavor production mainly arises from gluon fusion mechanisms, and is therefore sensitive to the initial gluon densities, which can in turn be modified by nuclear effects, such as shadowing. Thus, any comparison of heavy quarkonium production in different ion-ion collision systems or at different incident energies should take this "cold" nuclear effect into account. Therefore, the total heavy quark pair production should ideally be used as a reference for bound state yields.

- In heavy-ion collisions at CERN energies, the dilepton yield measured below the J/ψ invariant mass is above the sum of all the contributions expected from known sources [5,6]. Actually, the yield of continuum dimuons [6] is found to be compatible with an increase of charmed particle production from p+p to Pb+Pb collisions, that

is stronger than the simple scaling with the number of binary nucleon-nucleon collisions. It is not clear at present whether this trend is due to an increase of total charm production, a rescattering of charmed particles that would allow them to enter the detector acceptance, or a completely unknown source. However, a measurement of the total charm cross-section from p+p to Au+Au at RHIC energy is an important piece of information that can help to solve this puzzle.

- It has been observed that π^0 and charged hadron production is strongly suppressed [7] at high transverse momentum in Au+Au collisions at $\sqrt{s_{NN}} = 200$ GeV as compared to d+Au interaction at the same incident energy. This has been interpreted as the result of parton energy loss in the dense medium produced by the collision. This suppression has been predicted to be weaker for heavy quarks, due to the "dead cone" effect [8]. As for other particles, a "cold" nuclear matter effect is also to be taken into account, namely the "Cronin effect", which can modify the transverse momentum distributions of charmed hadrons due to initial parton-parton scattering.

- The anisotropy parameter v_2 and its transverse momentum dependence have been measured for light identified particles at RHIC. The results are compatible with a collective flow developing in the early stage of the collision [9]. It is therefore interesting to measure the possible anisotropy of heavy flavored particle emission.

In this paper, measurements of single electron distributions with the PHENIX detector at RHIC are presented. These measurements have been performed in p+p interactions at $\sqrt{s} = 200$ GeV, as well as with $\sqrt{s_{NN}} = 200$ GeV

d+Au and Au+Au, and $\sqrt{s_{NN}} = 62.4$ GeV Au+Au collisions. The contributions of electrons (e^\pm) from the decay of open charm and bottom particles have been extracted, and transverse momentum (p_T) distributions have been calculated and corrected for detector acceptance and efficiency effects.

Although this paper focuses on the measurement of single electrons, other heavy flavor signals are presently under study in PHENIX. This is the case of direct reconstruction of open heavy flavor particles, such as $D^0 \rightarrow K^- \pi^+$, which is very challenging due to the high multiplicity of secondary particles produced in heavy-ion collisions. Heavy flavor production is also under investigation using lepton pairs in the mass continuum, or electron-muon coincidences. In addition, heavy quark resonances have been studied via their decays into lepton pairs [10].

2 The PHENIX Apparatus

The PHENIX detector is shown in Fig. 1. It consists of four “arms”, each of which is made of several subsystems [11]. The North and South arms are dedicated to the detection and identification of muons in the forward and backward pseudorapidity regions $1.2 < |\eta| < 2.4$. The momentum of muons is determined from their deflection in the muon magnets, as measured with cathode strip chambers. In each muon arm, an identifier allows to detect muons in five layers of “Iarocci” drift tubes interleaved with four steel absorber plates (10, 10, 20 and 20 cm thick = 5.4 interaction lengths). Together with the central magnet and the muon magnet backplate, this leads to a minimum original energy of 1.9 GeV for a muon to reach the first layer and 2.7 GeV to penetrate completely through the identifier.

The central arms (East and West) are designed to track particles in the pseudorapidity range $|\eta| < 0.35$ ($70^\circ < \theta < 90^\circ$). Their azimuthal coverage is of 90° each. They consist of drift chambers (DCs), three layers of pad chambers (PCs), ring imaging Cherenkov counters (RICHs) and electro-magnetic calorimeters (EMCals). The EMCals are of two different types: lead-scintillator (PbSc) and lead-glass (PbGl). In the RICH, an array of photomultiplier tubes (PMTs) is used to detect the photons emitted by fast charged particles in the CO_2 gas radiator (the threshold is $p > 4.7$ GeV/c for pions). The DCs and PCs are used to reconstruct particle trajectories. The electron identification is performed by the RICHs, and the EMCals are used to measure the position and energy of photons and electrons. The central magnet produces a magnetic field that is parallel to the beam axis, and allows momentum analysis of charged particles.

In addition, a set of global detectors allows to characterize interactions. The beam-beam counters (BBCs), located ± 144 cm from the center of the interaction region, provide the reference time of the collisions, and the longitudinal position of the interaction vertex. They also provide the event trigger and the collision centrality. Each BBC comprises 64 quartz radiators and PMTs. Two zero-degree calorimeters (ZDCs) placed 18 meters upstream

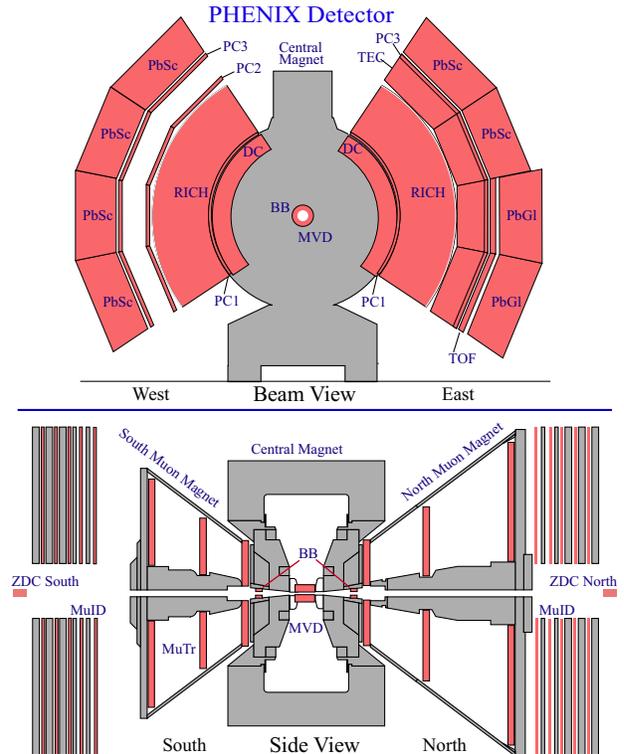


Fig. 1. Overview of the PHENIX central arm (top, transverse view) and muon arm (bottom, longitudinal view) detectors. The East and West arms azimuthal coverage is 90° , and their detector sets are slightly different. The muon arms are also not identical, the South muon tracker being shorter than the North one. Each muon tracker consists of 3 layers of cathode strip multiwire proportional chambers inserted in “lampshade” magnets. Muon identifiers are made of steel absorbers interleaved with 5 layers of (X,Y) Iarocci tubes.

and downstream of the central interaction point detect hadrons in the very forward regions ($|\eta| > 6.0$). They are used to measure the energy of the spectator neutrons.

3 Single Electrons

Electrons are detected in the central arm spectrometers ($|\eta| < 0.35$, see section 2). Charged particle tracks are reconstructed using DC and the first layer of PCs, together with the interaction vertex position determined using the BBCs. Track projection to the EMCal and the effective associated hit must match within 2 standard deviations. Matching is then required with a ring shaped signal in the RICH, comprising at least 3 hits. Using the energy measured by the EMCal the narrow electron peak at $E/p = 1$ is then selected by the following cut: $-2\sigma < (E - p)/p < 3\sigma$, where σ is the standard deviation of $(E - p)/p$. The remaining hadron contamination ($\simeq 10\%$) is subtracted using an event-mixing technique. The resulting single electron sample contains two main contributions, so-called “photonic” and “non-photonic”. The photonic part corresponds to Dalitz decays of light neutral

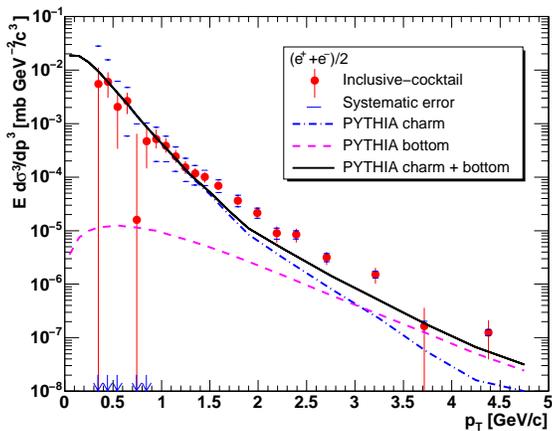


Fig. 2. Preliminary p_T distribution of non-photonic electrons measured in p+p collisions at $\sqrt{s} = 200$ GeV. The curves show the contributions from charm (dash-dotted curve) and bottom (dashed curve) decay, expected from PYTHIA calculations.

mesons (π^0 , η , η' , ρ , ω and φ) and photon conversions in the different detectors and materials. The non-photonic part mainly consists of electrons from semi-leptonic decay of open heavy flavor particles. A small contamination (a few %) arises from dielectron decays of light vector mesons and from kaon weak decay. The different contributions to the photonic electron spectrum, and the dielectron contribution have been calculated using a hadron decay generator [12]. In this “cocktail” method, photon conversions are evaluated using a detailed GEANT simulation. For some data samples, a complementary determination of the photonic component has been performed by introducing a thin (1.7% X_0) brass converter in the detector acceptance (at a distance $r = 29$ cm) during a fraction of the data taking period. A full GEANT simulation is also performed in both converter-in and converter-out configurations. The comparison between data obtained with the converter-in and converter-out configurations leads to a measurement of the contribution from photonic sources. All the details of this analysis method can be found in [13].

4 Results

4.1 Proton-Proton Collisions

The p+p data sample analyzed here has been recorded during RHIC run-2 operation, and consists of 15 M minimum-bias triggers and 420 M sampled minimum-bias triggers associated with an EMCal-RICH coincidence (ERT trigger). Photonic contributions are subtracted using the cocktail method as described earlier (see section 3), and all the spectra are corrected for acceptances and efficiencies.

Figure 2 shows the transverse momentum preliminary distribution of non-photonic single electrons obtained for p+p interactions. Background subtraction is the dominant contribution to the experimental systematic error. This

spectrum is compared to PYTHIA calculations including open charm and bottom contributions [14,12]. Background from Drell-Yan pairs and $J/\psi \rightarrow e^+e^-$ is found to be negligible. It is clearly seen that charm contribution alone does not reproduce the data at high p_T . Taking into account the contribution from open bottom, the agreement is better although still not perfect above 1.5 GeV/c [14,12,15]. The experimental distribution is indeed harder than expected from PYTHIA calculations, with parameters chosen as to reproduce lower energy data.

The total open charm cross-section is calculated from a fit using distribution shapes obtained with PYTHIA 6.205 and CTEQ5L PDFs for both charm and bottom contributions, allowing free normalization factors, as shown in Fig. 3. As detailed in [13], the PYTHIA charm ratios have been changed, using $D^+/D^0 = 0.45 \pm 0.1$, $D_s/D^0 = 0.258 \pm 0.1$, $A_c/D^0 = 0.1 \pm 0.05$, giving a c -quark $\rightarrow e$ total branching ratio of $9.5 \pm 0.4\%$. In the following, this fitted shape will be used to compare p+p results to those obtained in nucleus-nucleus collisions. The cross-section is then extrapolated from the central rapidity region to full phase space. In this calculation, other contributions are taken into account in the final systematic error, the most significant ones being the uncertainty on PYTHIA parameters (mainly $\langle k_T \rangle = 1.5 \pm 0.5$ GeV/c) and the choice of different parton distribution functions for the extrapolation. The full phase space cross-section is

$$\sigma_{c\bar{c}} = 709 \pm [85]_{stat} \pm [281]_{syst} \mu\text{b} \quad .$$

This value of total charm production cross-section is much lower than the one reported by STAR [16] from d+Au measurement: $1.4 \pm 0.2 \pm 0.4$ mb.

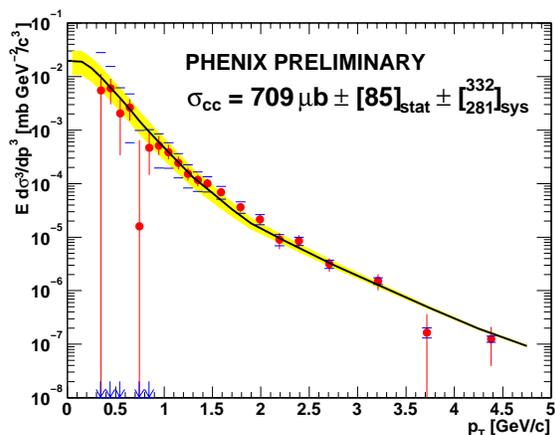


Fig. 3. Preliminary p_T distribution of non-photonic electrons measured in p+p collisions at $\sqrt{s} = 200$ GeV, together with the error band used to calculate the charm production cross-section. The PYTHIA lineshapes for electrons from charm and bottom contributions are added with the free normalizations that best fit the data (solid curve). The fit systematic error (shaded area) is calculated by offsetting the data by its systematic error and repeating the fit procedure.

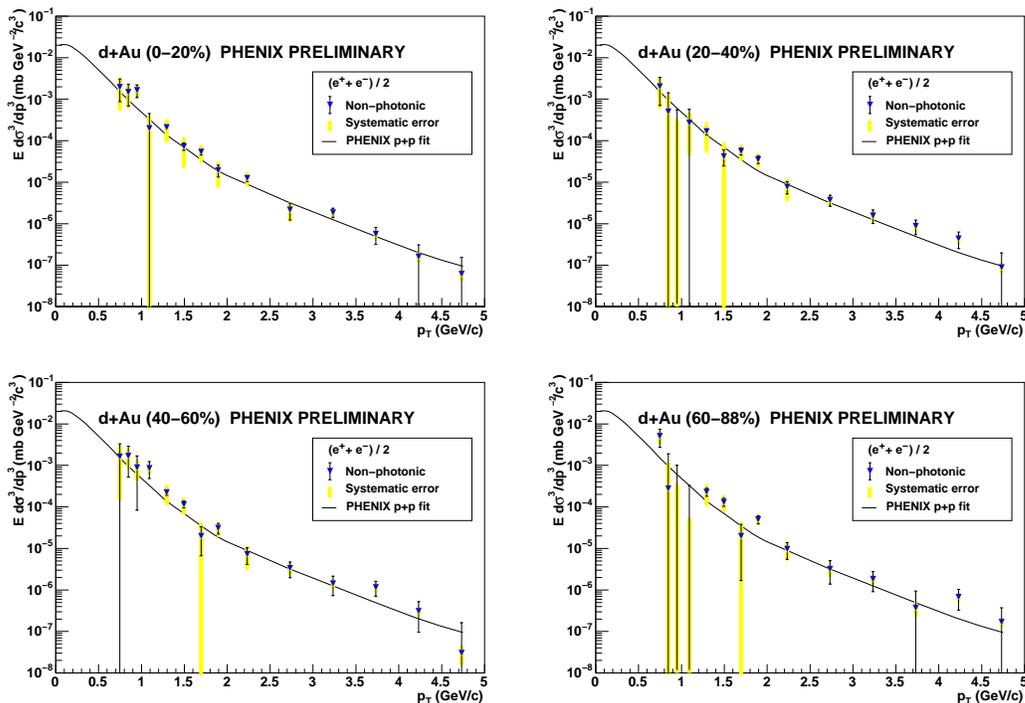


Fig. 4. Preliminary p_T distributions of non-photonic electrons, measured in four centrality classes of d+Au events at $\sqrt{s_{NN}} = 200$ GeV. All points are downscaled by the nuclear overlap function T_{AB} , to take into account the different number of binary nucleon-nucleon in each centrality class. The solid curves represent the best fit of p+p data, as shown in Fig. 3.

4.2 d-Au Collisions

Run-3 d+Au collisions are then used to investigate the effect due to modifications of parton distributions in the nuclear environment. The preliminary analysis described here uses the converter subtraction technique (see section 3), and 5 M (resp. 5 M) minimum-bias events plus 312 M (resp. 600 M) minimum-bias events sampled by the ERT trigger in the converter-in (resp. converter-out) configuration. The resulting non-photonic electron spectra are displayed in Fig. 4 in four centrality intervals [17]. All experimental distributions are downscaled by the nuclear overlap function T_{AB} to take into account the number of binary nucleon-nucleon collisions corresponding to the centrality class considered. The curve obtained with the best fit of the p+p data is superimposed, and is found to be in good agreement with d+Au results. From this comparison, we conclude that no strong cold nuclear matter effect is observed on heavy flavor production in the central rapidity region.

4.3 Au-Au Collisions

A similar analysis has been performed on RHIC run-2 Au+Au ($\sqrt{s_{NN}} = 200$ GeV) data, using the converter method to determine the photonic contribution to the electron yield (see section 3). Data samples consisted of 2.2 M (resp. 2.5 M) minimum bias events with the converter in (resp. out) [13]. The raw (photonic + non-photonic)

electron p_T spectra are shown in Fig. 5(a), for both configurations. Figure 5(b) shows both R_{CN} and R_γ , which are respectively the ratio of the raw distributions with converter in/out, and the multiplication factor of the photonic contribution that is due to the converter. R_γ is calculated by means of a full GEANT simulation with and without converter. All the details concerning this procedure can be found in [13]. The ratio of non-photonic to photonic electron yields is displayed in Fig. 5(c) as a function of p_T .

As for the d+Au analysis, the non-photonic electron spectra are downscaled by the nuclear overlap function T_{AA} and compared to p+p best fit, for different centrality intervals. As can be seen from Fig. 6, the agreement is quite good, although not perfect above $p_T = 2$ GeV/c, especially for central collisions. A new analysis with higher statistics [18] seems to indicate that the data points are systematically under the corresponding p+p curves for high p_T , which would reflect a suppression of non-photonic electrons at high p_T .

The non-photonic electron yield in the range ($0.8 < p_T < 4.0$ GeV/c), normalized to the number of binary nucleon-nucleon collisions (N_{coll}), is plotted in Fig. 7, as a function of N_{coll} . A fit of this yield to AN_{coll}^α leads to $\alpha = 0.938 \pm 0.075(\text{stat}) \pm 0.018(\text{syst})$ for Au+Au data alone, and $\alpha = 0.958 \pm 0.035(\text{stat})$ if the p+p data point is included. This value is compatible with $\alpha = 1$, which indicates that no medium effect can be seen within present statistical errors.

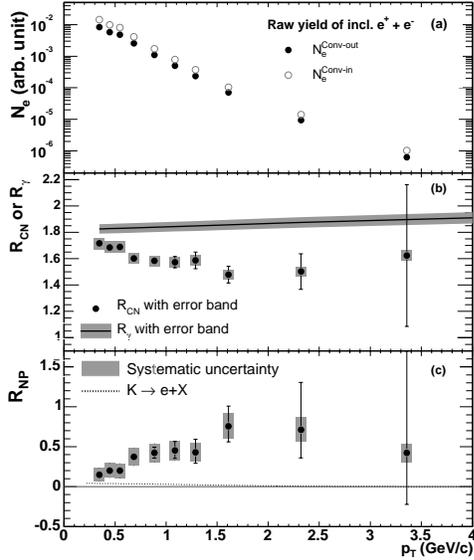


Fig. 5. Shown as a function of p_T : (a) raw (photonic + non-photonic) electron (e^\pm) spectra measured in the converter in (open circles) and out (closed circles) configuration (see text), (b) ratio of the converter in/out yields for inclusive (R_{CN}) and photonic (R_γ) electrons, (c) ratio of non-photon to photon electron yields.

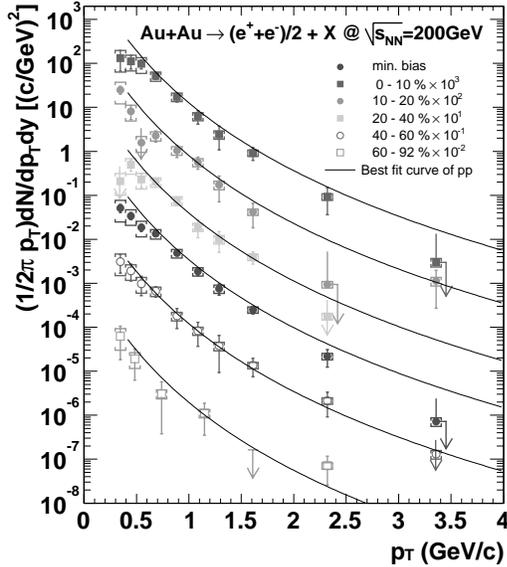


Fig. 6. p_T distributions of non-photonic electrons, measured in $\sqrt{s_{NN}} = 200$ GeV Au+Au collisions, for different centrality classes. Experimental results from successive centrality classes are scaled by factors of ten for clarity. The solid curve represents the best fit of p+p data (see Fig. 3), scaled by the nuclear overlap function T_{AA} . Best p+p curves seem to be systematically above Au+Au data at high p_T , although it is difficult to draw any conclusion within present statistical error. A more recent analysis with full statistics [18] shows this trend more clearly.

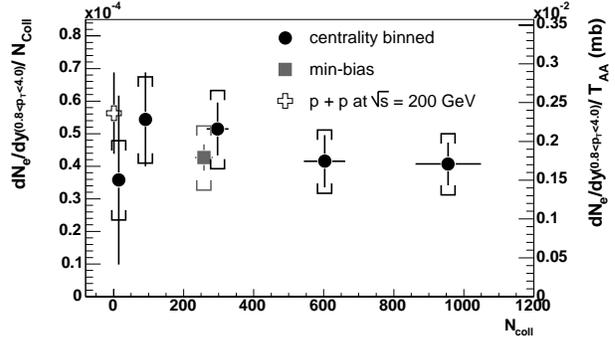


Fig. 7. Non-photonic electron yield ($0.8 < p_T < 4.0$ GeV/c) measured in $\sqrt{s_{NN}} = 200$ GeV Au+Au collisions, scaled by the number of binary nucleon-nucleon collisions (N_{coll}), as a function of N_{coll} . The right-hand scale corresponds to electron cross-section per nucleon-nucleon collision.

Au+Au ($\sqrt{s_{NN}} = 62.4$ GeV) data have also been analyzed. The resulting non-photonic electron spectrum is compared to existing p+p ISR data at the same incident energy [19]. This comparison is shown in Fig. 8. The experimental points are calculated for the minimum-bias (0-83.4%) centrality class. All the p+p ISR data are scaled by a factor $T_{AB} = 6.94$ mb $^{-1}$, corresponding to an average number of binary collisions $\langle N_{coll} \rangle = 256.6$. Within experimental errors, no deviation can be seen from binary collision scaling at this incident energy.

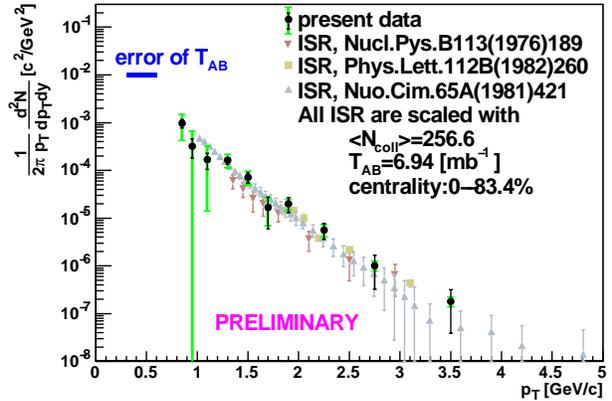


Fig. 8. Preliminary p_T distributions of non-photonic electrons, measured in $\sqrt{s_{NN}} = 62.4$ GeV Au+Au collisions. Comparison with ISR p+p data at the same incident energy shows that the present data is compatible with N_{coll} scaling.

5 Elliptic flow of non photonic electrons

The anisotropy v_2 parameter of non-photonic electron distributions has also been measured in Au+Au collisions at $\sqrt{s_{NN}} = 200$ GeV [20]. In this analysis, 16 M minimum bias events from RHIC run-2 have been considered.

The reaction plane is deduced from the signals measured by the BBCs (see section 2) in the pseudorapidity range $3.1 < \eta < 3.9$. The resulting v_2 distribution as a function of p_T is shown in Fig. 9. In the intermediate p_T region ($1.0 < p_T < 1.7$ GeV/c), the anisotropy parameter v_2 is non-zero with a 90% confidence level [20]. The curves correspond to two model calculations which assume very different scenarios [21]: no reinteraction of the heavy quarks after their production by initial state hard processes (solid), or complete thermalization (dashed). The present systematic and statistical uncertainties prevent from discriminating between these scenarios.

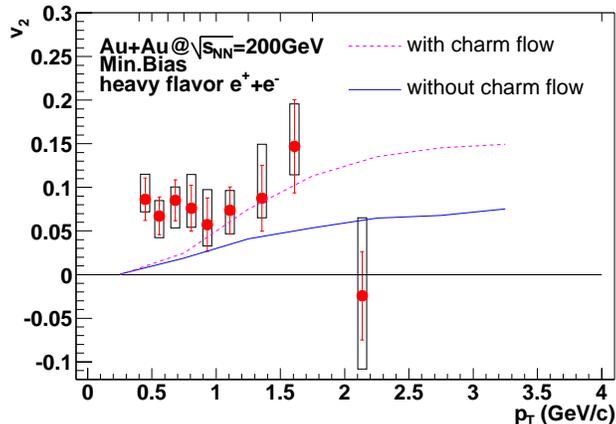


Fig. 9. Transverse momentum dependence of the heavy flavor electron v_2 parameter, measured in $\sqrt{s_{NN}} = 200$ GeV Au+Au collisions. The solid line represents the initial charm contribution without any rescattering, whereas the dashed line shows the effect of flow and complete thermalization.

6 Conclusion

Phenix has measured the production of single electrons (e^\pm) at RHIC, in the central rapidity region, for p+p, d+Au and Au+Au collisions at $\sqrt{s_{NN}} = 200$ GeV, as well as for Au+Au interactions at $\sqrt{s_{NN}} = 62.4$ GeV. The contribution of open heavy flavor (mainly charm) particle semi-leptonic decay has been calculated from these measurements, after subtraction of the photonic electron component, for different centrality classes of ion+ion collisions. The total charm cross-section has been calculated from p+p data. From p+p to d+Au and Au+Au collisions, the total yield of electrons from charm decay is consistent with N_{coll} scaling, where N_{coll} is the number of binary nucleon-nucleon collisions corresponding to the centrality class considered. The p_T distributions of electrons from charm decay measured in nucleus-nucleus collisions are correctly reproduced by the curve obtained from p+p best fit, although a more recent analysis with full statistics seems to indicate a suppression of electrons from charm decay at high p_T in Au+Au collisions at $\sqrt{s_{NN}} = 200$

GeV. Au+Au data measured at $\sqrt{s_{NN}} = 62.4$ GeV agree with ISR p+p data scaled by the number of binary collisions. The anisotropy parameter v_2 of single electrons from heavy flavor decay is found to be non-zero, although present uncertainties do not allow to draw any conclusion about charm flow.

References

1. T. Matsui and H. Satz, Phys. Lett. **B178** (1986) 416.
2. A. Andronic *et al.*, Phys. Lett. **B571** (2003) 36, M. Gorenstein *et al.*, J. Phys. **G28** (2002) 2151, R. Thews *et al.*, Phys. Rev. **C63** (2001) 054905.
3. B. Alessandro *et al.*, Eur. Phys. J. **C39** (2005) 335.
4. S. Adler *et al.*, Phys. Rev. **C69** (2004) 014901.
5. G. Agakishiev *et al.*, Phys. Lett. **B422** (1998) 405.
6. M.C. Abreu *et al.*, Eur. Phys. J. **C14** (2000) 443.
7. S. Adler *et al.*, Phys. Rev. **C69** (2004) 034910, B. Back *et al.*, Phys. Rev. Lett. **91** (2003) 072302, S. Adler *et al.*, Phys. Rev. Lett. **91** (2003) 072303, J. Adams *et al.*, Phys. Rev. Lett. **91** (2003) 072304, I. Arsene *et al.*, Phys. Rev. Lett. **91** (2003) 072305.
8. Y. Dokshitzer and D. Kharzeev, Phys. Lett. **B519** (2001) 199.
9. S. Adler *et al.*, Phys. Rev. Lett. **91** (2003) 182301, J. Adams *et al.*, Phys. Rev. Lett. **92** (2004) 052302.
10. M. Rosati *et al.*, these proceedings.
11. The PHENIX detector overview can be found in: K. Alcox *et al.*, Nucl. Instr. Meth. **A499** (2003) 469, followed by the detailed descriptions of the different subsystems in the same volume.
12. K. Adcox *et al.*, Phys. Rev. Lett. **88**, (2002) 192303.
13. S. Adler *et al.*, nucl-ex/0409028.
14. S. Kelly (PHENIX Collaboration), J. Phys. **G30**, (2004) S1189.
15. R. Averbeck (PHENIX Collaboration), J. Phys. **G31**, (2005) S259.
16. J. Adams *et al.*, Phys. Rev. Lett. **94** (2005) 062301.
17. S. Adler *et al.*, nucl-ex/0411054.
18. S. Butsyk (PHENIX Collaboration), 21st Winter Workshop on Nuclear Dynamics, Breckenridge, CO, Feb. 5-12, 2005.
19. T. Tabaru (PHENIX Collaboration), International Conference on Physics and Astrophysics of Quark Gluon Plasma, Kolkata, India, Feb. 8-12, 2005.
19. F.W. Busser *et al.*, Nucl. Phys. **B113** (1976) 189, P. Perez *et al.*, Phys. Lett. **B112** (1982) 260, M. Basile *et al.*, Nuovo Cim. **A65** (1981) 421.
20. S. Adler *et al.*, nucl-ex/0502009.
21. V. Greco *et al.*, Phys. Lett. **B595**, (2004) 202.